International Journal of Electrical and Computer Engineering (IJECE)
Vol. 16, No. 1, February 2026, pp. 174~186
ISSN: 2088-8708, DOI: 10.11591/ijece.v16i1.pp174-186

Microbubble size and rise velocity measurement in dissolved air flotation system

Jeimmy Adriana Muñoz Alegría[1,2], Jesús Emilio Pinto-Lopera[3], Elena Muñoz-España[1], Juan Fernando Flórez-Marulanda[1]
[1]Department of Electronics, Instrumentation and Control, Faculty of Electronic Engineering and Telecommunications, Universidad del Cauca, Popayán-Cauca, Colombia
[2]Doctorate in Energy, Water and Environment, University of La Serena, La Serena, Chile
[3]Faculty of Engineering, Universidad de la Amazonia, Florencia-Caquetá, Colombia

Article Info

Article history:

Received Nov 12, 2024
Revised Sep 27, 2025
Accepted Nov 23, 2025

Keywords:

Camera calibration
Computer vision
Dissolved air flotation
Microbubble tracking
Rectangular dissolved air flotation
Video processing
Wastewater treatment

ABSTRACT

Water reuse and resource recovery are priority environmental goals under increasing water scarcity and climate stress. Dissolved air flotation (DAF) is widely applied in municipal, industrial, and decentralized treatment trains because fine microbubbles (MB) enhance solids removal efficiency. Accurate, low-cost characterization of MB size and rise velocity is therefore valuable for process monitoring and optimization. This study develops and validates a smartphone-based, computer-vision pipeline for laboratory-scale DAF systems. After camera calibration and lens un-distortion, each video sequence (235 frames per run) is processed through grayscale conversion, median, Gaussian, and local-Laplacian filtering, gamma correction, and Otsu thresholding, followed by morphological refinement. Circular Hough transform then identifies MB candidates, providing their diameters and centroid locations. These detections are then linked frame-to-frame using a distance-gated nearest-neighbor tracker with dynamic memory allocation to accommodate new MBs under turbulent, bubble-clustering conditions. Rise velocity is computed from interframe centroid displacement and frame interval. The system reliably tracked up to 32 microbubbles simultaneously per video. Across four operating pressure/airflow combinations, mean MB diameters ranged 95.47–216.42 µm and mean rise velocities 9.40×10^{3}–2.76×10^{4} µm/s. The approach is low cost, computationally lightweight, and suitable for rapid MB characterization to support DAF monitoring, optimization, and research.

Corresponding Author:

Jesús Emilio Pinto-Lopera
Facultad de Ingeniería, Universidad de la Amazonia
Sede Porvenir Calle 17 Diagonal 17 con Carrera 3F, Florencia-Caquetá 180002, Colombia
Email: jes.pinto@udla.edu.co

1. INTRODUCTION

Pollution and freshwater scarcity are pressing global issues, particularly in light of climate change. Likewise, global water demand is projected to increase by 20% to 30% annually by 2050 [1]. In this regard, the combined industrial and energy sectors extract 19% of the world's freshwater, agriculture accounts for 69%, and municipal domestic water represents 12% of global water extraction. According to a United Nations report, 44% of domestic wastewater is not treated correctly [2]. It estimates that approximately 380 billion cubic meters of water can be recovered from the annual volumes of wastewater produced. By 2030, 470 billion cubic meters are expected to be recovered, and 574 billion cubic meters by 2050 [3]. On the other hand, various wastewater treatment technologies exist, where systems based on the dissolved air

flotation (DAF) technique stand out. In this regard, flotation using air or gas bubbles is one of the most commonly applied physicochemical techniques today due to its high efficiency in removing fine and ultrafine particles, emulsions, oils, fats, turbidity, organic matter, and microorganisms [4]–[8], which has increased its demand in recent years [9]–[12].

In DAF systems, bubbles are classified into macro-bubbles for diameters between 2 and 5 mm, microbubbles (MB) for diameters between 1 and 100 μm, and nanobubbles (NB) or ultra-fine bubbles with diameters < 1 μm [13]–[15]. Here, microbubbles exhibit unique properties that allow for better mass transfer due to the increased mass transfer area, longer residence time, and lower coalescence potential [13], [15], [16]. These properties facilitate effective contact between particles and microbubbles in flotation [17]–[19]. In contrast, macro-bubbles tend to float rapidly, resulting in low removal efficiency [20], [21]. Thus, the primary characteristic parameters of microbubbles in DAF systems are diameter and rise velocity, due to their significant impact on removal effectiveness. The decrease in bubble size increases the contact angle and the adhesion force of the particle [19]. Consequently, it allows for more opportunities for collision with suspended particles and better cleaning, thus increasing the effectiveness of the flotation process [17]–[19], [22]. However, in wastewater treatment, various factors affect the MB size and rise velocities, such as surfactants, coagulants, or chemical additives that facilitate the removal of contaminants [23]. Therefore, bubble characterization provides valuable information to ensure efficient cleaning in wastewater treatment [21], [24]–[26].

In this regard, various techniques have been developed to determine the characteristic parameters of MB, ranging from intrusive to non-intrusive methods, with digital image processing (DIP) being a notable example among the latter [27]. However, detecting MB in industrial environments remains a challenge for researchers due to the complex relationship between shape, size, turbulence, surrounding forces, the physicochemical medium in which they are contained, overlap, and MB concentration [13]. Additionally, since microbubbles are transparent objects and lighting conditions within processing machines are challenging, their appearance may be affected during measurement, which would pose a significant problem. In attempting to solve this problem, increasingly sophisticated algorithms have been developed, such as convolutional neural network (CNN) methods, which offer greater object detection robustness [28]. For example, in [29], bubbles were detected as circular objects using CNN, outperforming other methods in detection and providing an accurate estimation of size distribution. However, the process is slow, making it unsuitable for real-time use. Gulden *et al.* [17] developed an online bubble size analysis technique based on DIP to evaluate the performance of a laboratory DAF device operating under ideal conditions at a saturation pressure of 58 psi and a recirculation flow rate of 100 L/h. Image processing relies on binarization techniques, edge detection, and the Hough transform. This work enabled the recognition of overlapping bubbles but had limitations in identifying small individual bubbles. Therefore, it complemented the processing with additional algorithms that address this issue with specific adjustments.

In this regard, bubble overlapping becomes another complex issue to address when the MB concentration is high. For this, algorithms such as the Hough transform and Watershed, among others, have been implemented to segment overlapping bubbles and attempt to extract their characteristics [17], [30]–[33]. Study [34] addresses the segmentation of overlapping bubbles, showing up to 95% effectiveness when overlapping bubbles do not exceed 50% of the sample in each analyzed image. Additionally, the bubble identification technique requires tracking bubbles frame by frame in a sequence, allowing the path of each bubble to be traced and counted if they are obstructed by overlap. The work indicates that each bubble should be isolated at least once in a photo during the sequence. On the other hand, there is also more specialized instrumentation that assists in MB characterization, ranging across a wide variety of equipment, from optical microscopes [31], [35] and electron microscopes [36], [37], to laser diffraction devices like the Spraytec [15], the McGill bubble size analyzer (MBSA) [19], [38], or unconventional methods such as the monofiber optical probe [39], and electrical resistance tomography [40], [41], atomic force microscopy [42]. However, this instrumentation is expensive and limited to specialized laboratories.

The objective of this study is to develop and validate a cost-effective computer vision methodology capable of accurately characterizing overlapping microbubbles in the highly turbulent, rectangular-tank DAF configuration. To that end, a low-cost imaging pipeline is proposed that combines a smartphone camera calibrated with a chessboard target and a Venturi-based MB generator driven by a *Pedrollo CP660* pump. The algorithm i) extracts frames at 960 fps, ii) performs sequential grayscale conversion, multi-stage filtering, Otsu segmentation, and morphological cleanup, and iii) resolves bubble overlap through a Euclidean-distance tracking routine and circular Hough detection. With this approach, the influence of recirculation flow (900 L/h) and saturation pressure (34–36 psi) on MB diameter and rise velocity is quantified: the 36 psi / 0.1 L/min condition yields the smallest mean diameter (~99 μm) and the lowest mean velocity (~9.9×10^3 μm/s). The results demonstrate that the proposed low-cost system achieves performance comparable to that of high-speed industrial setups while directly addressing bubble overlap—a limitation of previous work—and thus offers practical potential for real-time DAF monitoring and optimization.

2. METHOD

2.1. Experimental setup

The experimental setup primarily comprises a laboratory-scale DAF system, an imaging acquisition system that includes a camera, and a computational system with the processing algorithm. The DAF system consists of a rectangular glass tank with a thickness of 1 cm, which facilitates the visualization of interest objects, a microbubble generator device, and a Venturi tube based on the physical principle of hydrodynamic cavitation, designed as specified in [43]. A maximum flow rate of 16 liters per minute circulates through it, operating at an ambient temperature of between 25 °C and 27 °C. A conventional 2 HP water pump (Pedrollo CP660) enables water circulation through the hydraulic circuit, with flow rates ranging from 20 to 130 L/min.

The tank has dimensions of 52 cm in height, 25 cm in width, and 75 cm in length, with an internal partition to facilitate visualization of the MB and the hydrodynamics during the cleaning process as shown in Figure 1. The setup includes the contact, separation, sludge collection, and MB visualization zones. In the contact zone, the microbubbles separate the contaminating substances, which subsequently float to the tank's surface, forming a layer of foam or sludge that is removed by overflowing into the sludge collection zone. In this area, microbubbles are introduced with recirculation pressures of 34 and 36 psi, and air injection rates of 0.1 and 0.5 L/min, serving as operational parameters of the DAF system. A baffle with an approximate height of 20 cm and an angle of 53° divides the DAF tank into a separation zone, where the water that has passed through the cleaning process via the MB is held. A portion of this water is used for recirculation, while another portion exits for other cleaning processes. Finally, the MB visualization zone is lined with black paper on the tank's side walls to distinguish the microbubbles from the background and prevent reflections from external objects.

Figure 2 summarizes the experimental arrangement used in this work. Figure 2(a) shows the complete bench comprising the external water reservoir, the rectangular DAF unit (contact and separation zones) and the associated piping, pump and injector; Figure 2(b) depicts the image-acquisition setup: a Huawei P30 (ELE-L04) smartphone fitted with a 15× external macro lens, mounted on a tripod and focused on the viewing window of the DAF tank. A 7 W white backlight placed behind the tank enhances bubble contrast for reliable detection and tracking. Videos were recorded at 720×1280 pixels and 960 frames per second; the effective working distance of the lens system was ~7 cm.

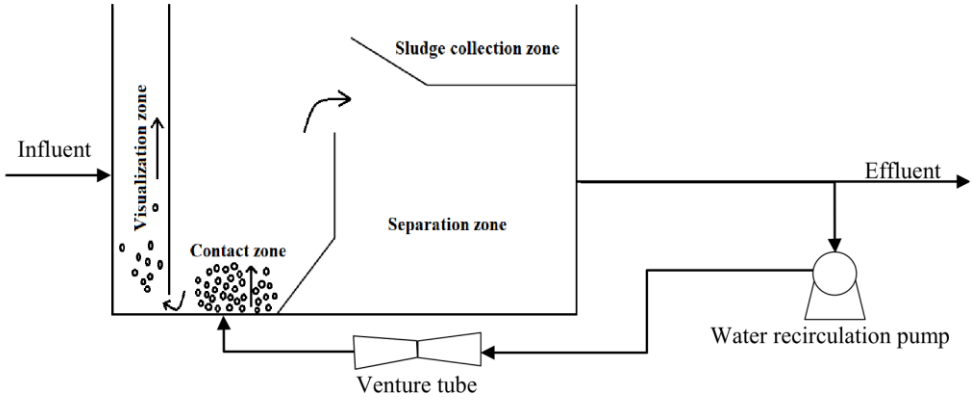

Figure 1. DAF experimental setup

(a) (b)

Figure 2. Experimental setup and imaging system (a) full laboratory bench: external water tank, DAF unit, and piping and (b) smartphone-based image acquisition with macro lens and rear illumination

The experiment to validate the algorithm that estimates the diameter and ascent velocity of the microbubbles was based on a 2×2 factorial experiment as shown in Table 1, in which the operational parameters of recirculation pressure were varied to 34 psi and 36 psi, and air injection was set at Q1=0.1 L/min and Q2=0.5 L/min. Ten videos were recorded for each treatment, each lasting approximately 10 seconds, with a 20-second interval between recordings to ensure the detection of different microbubble populations per video. A total of 40 videos were obtained for algorithm validation.

Table 1. 2×2 Experimental design for microbubbles generation at a flow rate of 900 L/h

Experiment	Air injection rates [L/min]	Saturation Pressure [psi]
A	0.1	34
B	0.5	34
C	0.1	36
D	0.5	36

2.2. Camera calibration

Instrument calibration is essential for accurate image acquisition in vision-based measurement systems. Camera calibration methods are commonly grouped into three-dimensional (3D), two-dimensional (2D), and one-dimensional approaches, each differing in the amount of scene geometry required and the level of accuracy achievable [44]. For imaging sensors, intrinsic and extrinsic parameters, as well as lens optical properties, introduce geometric distortions that can degrade quantitative measurements if uncorrected [45]. Estimating intrinsic parameters from correspondences between three-dimensional world points and two-dimensional image points enhances measurement fidelity; however, the ultimate accuracy of a calibration depends strongly on the reliability of feature detection in the calibration target [44].

In this study, camera calibration was performed in MATLAB using the “Camera Calibration” application with a 310-square chessboard target (5×5 mm squares). A total of 40 calibration images were acquired inside the DAF tank, ensuring that the optical path during calibration matched the experimental imaging conditions; the application automatically excluded defective images. Images were captured at multiple orientations (tilt angles < 45° relative to the camera plane, per application guidance) with autofocus disabled and zoom fixed at 3× to maintain geometric consistency across views. The application estimated the camera's intrinsic and extrinsic parameters. It generated a parameter file, which we incorporated into our preprocessing pipeline using MATLAB's '*undistortImage*' function to remove lens distortion from all experimental frames. The resulting calibration achieved an overall mean reprojection error of 1.83 pixels in the water-filled tank as shown in Figure 3, which we deemed acceptable for downstream measurements of microbubble size and position.

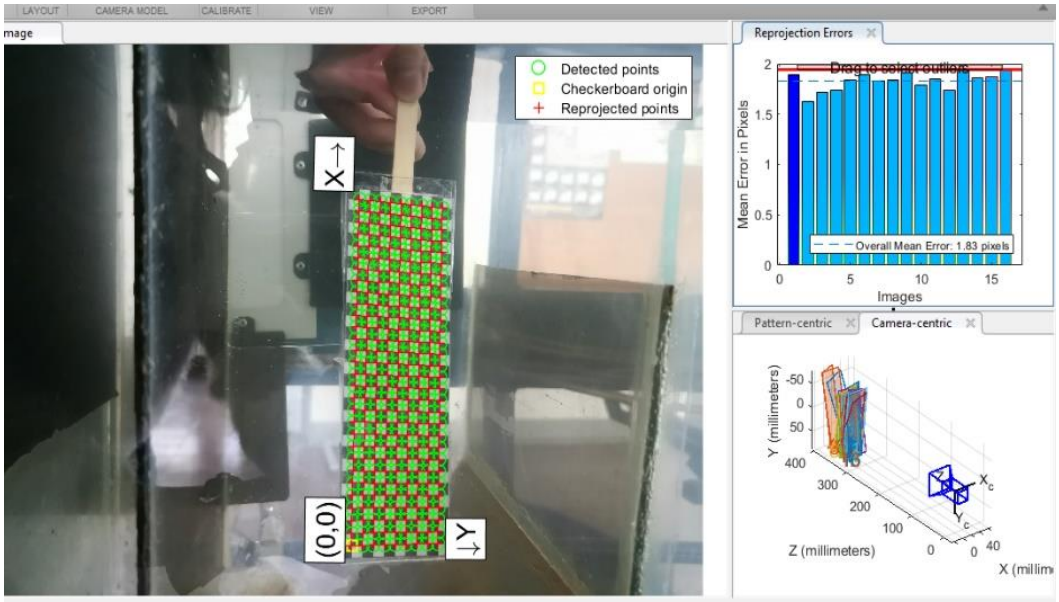

Figure 3. Estimation of the overall mean error in calibration using MATLAB

The intrinsic matrix of the camera and the final distortion factors (k) in this case:

$$A = \begin{bmatrix} f_x & 0 & 0 \\ s & f_y & 0 \\ c_x & c_y & 1 \end{bmatrix} = \begin{bmatrix} 3.8762 \times 10^3 & 0 & 0 \\ 0 & 3.8944 \times 10^3 & 0 \\ 1.8399 \times 10^3 & 1.4461 \times 10^3 & 1 \end{bmatrix} \quad (1)$$

$$k = [0.3543 \quad -2.7778]^T \quad (2)$$

The distortion coefficients k indicate that the camera operates with effectively square pixels; substantial departures of the sensor aspect ratio f_y/f_x from unity would imply non-square sampling. In our calibration, f_y/f_x =1.005, confirming near-square geometry for metric measurements. After establishing the geometric calibration, we determined the pixel-to-length conversion factor using the procedure outlined in [23], which involves a reference object of known diameter. A semi-transparent nylon filament (nominal diameter 600 µm) was mounted transversely over a black background, and several transverse cuts were made along the filament to provide multiple repeatable measurement points. Ten reference images were acquired with the camera-lens system at a resolution of 3648×2736 (manual focus, 3× zoom, ISO 200, 1/400 s shutter speed, F/1.8 aperture, 35 mm focal length equivalent). Filament diameters (in pixels) were extracted using the circular Hough transform, and the resulting spatial scale factor was computed as 1 pixel=5.79 µm.

2.3. Image processing algorithm

Figure 4 illustrates the image processing sequence used to extract microbubble diameters and centroid positions from each video. For each experiment, the camera was set to 960 fps, and within each video, windows of 235 consecutive frames were analyzed to compute MB diameter and rise velocity. Starting with the RGB frame converted to grayscale as shown in Figure 4(a), the workflow applies sequential noise-attenuation and contrast-enhancement operations as shown in Figure 4(b): median filtering (7×7 kernel) to suppress salt-and-pepper noise, Gaussian filtering (σ=2.6) provides additional smoothing, helping to mitigate additive noise. A local Laplacian filter then amplifies local contrast and accentuates MB edges, followed by a final gamma-based contrast boost. The enhanced image is segmented using Otsu's method, after which morphological refinement—dilation and erosion with orthogonal linear structuring elements plus edge cleanup—removes residual artefacts and closes gaps in MB regions as shown in Figure 4(c).

Although watershed segmentation is often applied to bubble populations with mixed geometries [32], [46], [47], it frequently leads to over-segmentation [20], [25], [31] and entails higher computational cost [25], [32], [48]. In this work, Otsu thresholding followed by morphological refinement is employed; the resulting binary image is then analyzed using the circular Hough transform to locate microbubble boundaries and centroid positions as shown in Figure 4(d). These centroid coordinates serve as the input for the displacement and rise velocity calculations (adapted from [49]) detailed in Figure 5 and (3) and (4). Here, two consecutive frames determine the distance traveled by the microbubble centroids. In this case, the position of the centroids changes when the microbubbles move. For example, Figure 5 shows that, in Frame 1, the centroid of a microbubble is defined as C_1, with coordinates (X_1, Y_1) and position vector $\overrightarrow{P_1}$. In Frame 2, the coordinates of the centroid for the same microbubble are (X_2, Y_2), and the position vector is $\overrightarrow{P_2}$. Based on these two position vectors, the displacement magnitude D is calculated using the Euclidean distance formula (3). Finally, the rise velocity, V_{MB}, of the microbubble is determined by (4).

$$D = \sqrt{(X_2 - X_1)^2 + (Y_2 - Y_1)^2} \quad (3)$$

$$V_{MB} = D/t_f \quad (4)$$

Where t_f is the time between consecutive frames. In this study, the camera was configured to record at 960 fps, yielding $t_f = 1.04\,ms$. This procedure is applied to all microbubbles in each consecutive video frame. Similar to clustering techniques like K-means, this method allowed tracking the microbubbles by identifying the coordinates of their centroids. Figure 6 presents a flowchart of the complete pipeline, highlighting three processing stages: i) data loading, with frame extraction from the original video, where *N* denotes the number of frames; ii) image pre-processing (grayscale conversion and application of median, Gaussian, Laplacian filters, and gamma correction); and iii) detection and measurement, in which—after Otsu segmentation and morphological operations—the circular Hough transform provides centroid positions that feed diameter estimation and subsequent rise velocity computation. Table 2 shows list the image-processing parameters used.

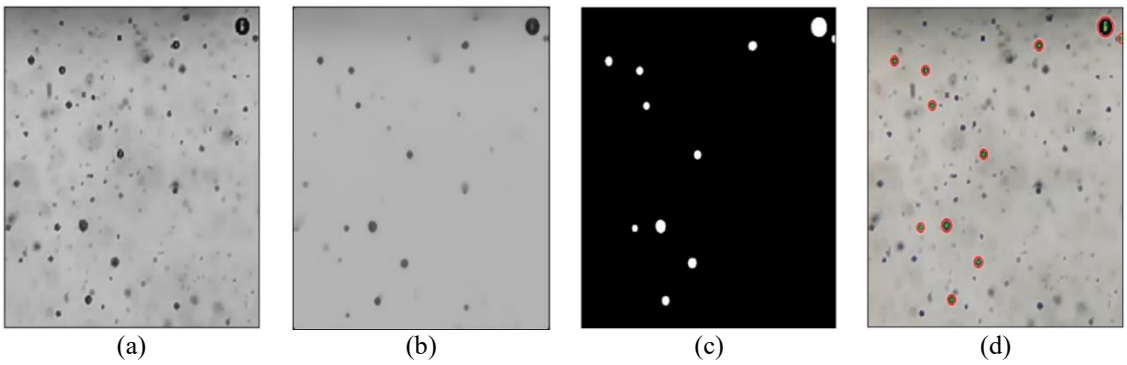

Figure 4. Image processing sequence (a) grayscale conversion, (b) filtering and contrast enhancement, (c) segmentation and morphological refinement, and (d) Hough-based MB feature extraction

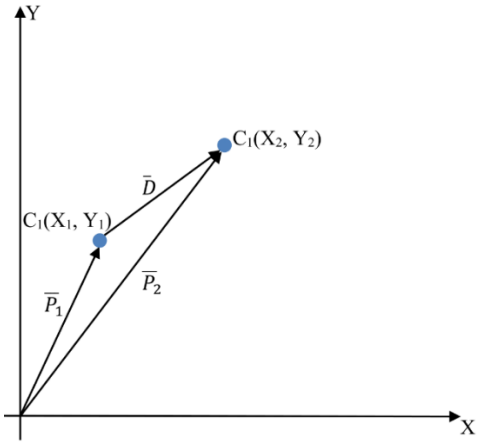

Figure 5. Representation of a microbubble displacement and its associated vectors

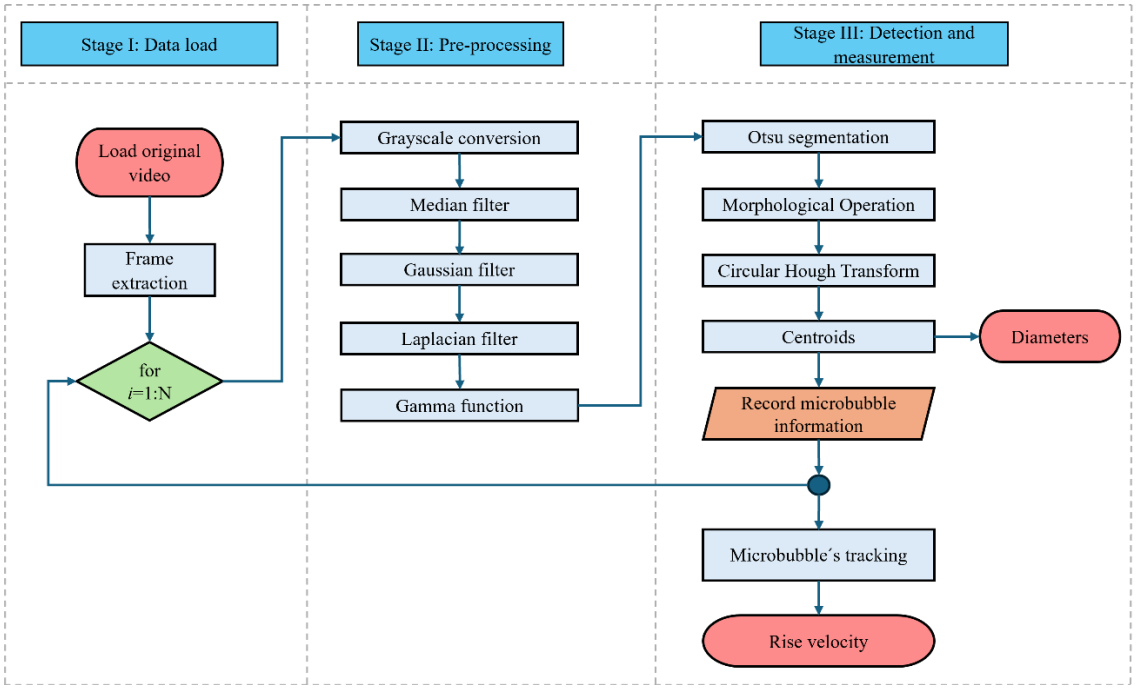

Figure 6. Flowchart of the image-processing pipeline

Table 2. Algorithm-configuration parameters

Processing stage	Process implemented	Parameter	Value/setting
Data loading	Frame extraction	Frame rate	960 fps
		Frames analyzed	235 consecutive frames
Pre-processing	Grayscale conversion	Color space	RGB → intensity
	Median filter	Kernel size	7×7 pixels
	Gaussian filter	σ (std. dev.)	2.6 pixels
	Local Laplacian	MATLAB parameters	sigma=0.12, alpha=9
	Gamma correction	Linear stretch	Range [0.3 1]
Detection and measurement	Otsu threshold	Adaptive global	Auto
	Morphology	Structuring elements	Lines length 3 pixels (erosion) and 4 pixels (dilation)
	Circular Hough transform	Radius range	5–20 pixels
		Sensitivity	0.9
	Spatial-scale calibration	Pixel-scale factor	5.79 µm/pixel

2.4. Microbubble tracking

Microbubble trajectories were reconstructed across consecutive processed frames. For each frame pair, the algorithm links microbubble centroids using a nearest-neighbor rule based on the minimum Euclidean distance between a centroid in the current frame (t) and all centroids detected in the next frame $(t+1)$; the match with the smallest distance is provisionally assigned as the continuation of that microbubble (3). This pairwise association is repeated for all centroids in the frame, producing a preliminary mapping from Frame 1 to Frame 2, Frame 2 to Frame 3, and so on through the whole image sequence of each experiment.

The frame-to-frame linking procedure is iterated across all 235 processed frame windows. This approach helps manage temporary clustering and partial occlusion events created by turbulence and recirculating flows in the DAF tank. Table 3 shows that the algorithm successfully tracked as many as 32 microbubbles simultaneously in individual videos, even under variable working pressures that increased fluid agitation. To focus on buoyant transport behavior, only microbubbles that moved from the lower to the upper region of the frame sequence were retained for analysis. When overlapping occurred, microbubbles were tracked so long as their centroids were separable in the first processed frame of the video; thereafter, the nearest-neighbor linkage preserved their identities across frames unless complete merging persisted over multiple frames.

Newly entering microbubbles between consecutive frames can disrupt tracking if not handled explicitly, because their centroids may i) overwrite the coordinates of previously tracked microbubbles or ii) be omitted altogether when array dimensions are fixed. To mitigate this, the tracking routine allocates expandable (dynamic) data structures for centroid storage, appending new microbubble IDs as they appear rather than reusing existing indices. Before linking, the algorithm checks whether candidate matches exceed a distance gate; if so, a new trajectory is initialized instead of overwriting an existing one. This strategy preserves established tracks, accommodates new arrivals, and prevents loss of centroid data in high-throughput sequences.

Table 3. Tracked microbubbles at different experiments. Each one is related to Table 1

Experiment	Processed videos									
	1	2	3	4	5	6	7	8	9	10
	Number of microbubbles detected by video									
A	21	17	27	17	18	18	9	13	11	15
B	12	20	32	12	32	20	20	27	24	21
C	25	21	30	21	25	26	20	15	9	27
D	11	16	16	8	9	12	8	12	7	14

3. RESULTS AND DISCUSSION

Microbubble size and rise-velocity responses were quantified for four operating conditions (Experiments A–D) that combined recirculation pressure and injected airflow rate as shown in Table 1. These responses were processed using the algorithm settings summarized in Table 2. The 34 psi/ 0.1 L/min condition is presented first to illustrate the data outputs, including diameter and rise-velocity histograms (Figures 7 and 8). Results for the remaining operating conditions are then compared, and overall trends are summarized to identify ranges that favor the generation of smaller-diameter, slower-rising MBs. Under 34 psi recirculation pressure and an airflow rate of 0.1 L/min (Experiment A), MB diameters spanned approximately 70–200 µm, yielding a mean of 117.34 µm with a standard deviation of 28.30 µm as shown

in Figure 7. The corresponding rise velocities ranged from 0.1×10⁴ to 3.5×10⁴ µm/s, with a mean of 1.35×10⁴ µm/s and a standard deviation of 7.58×10³ µm/s as shown in Figure 8. Most MBs in this condition clustered between ~85 and 140 µm (modal ~90–105 µm) and exhibited a positively skewed diameter tail with occasional larger bubbles; rise velocities likewise concentrated below ~1.8×10⁴ µm/s (modal ~0.7–1.2×10⁴ µm/s) with sparse high-velocity outliers, patterns consistent with intermittent coalescence and localized turbulent acceleration in the DAF flow.

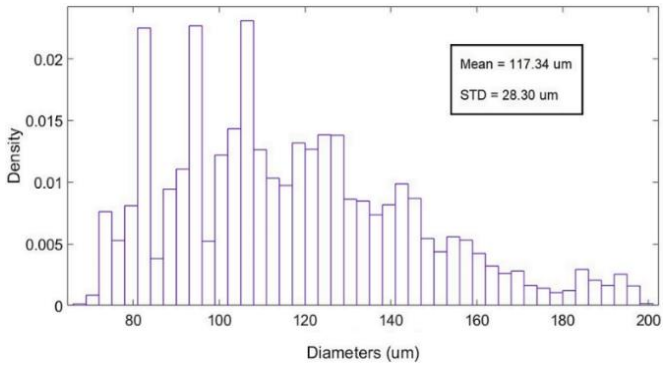

Figure 7. Microbubble diameters in experiment A

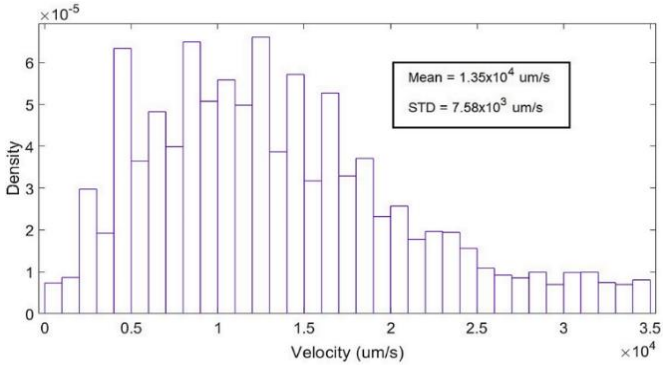

Figure 8. Microbubble rise velocity in experiment A

Experiment B (34 psi; 0.5 L/min) produced larger MBs, 100–400 µm in diameter (mean 165.32 µm; SD 65.42 µm), with rise velocities of 0.5×10⁴–3.5×10⁴ µm/s (mean 2.04×10⁴ µm/s; SD 6.79×10³ µm/s). Increasing pressure to 36 psi while holding airflow at 0.1 L/min (Experiment C) reduced MB diameters to 50–150 µm (mean 98.65 µm; SD 20.41 µm) and yielded rise velocities of 1×10⁴–2.5×10⁴ µm/s (mean 9.89×10³ µm/s; SD 4.97×10³ µm/s). At 36 psi with 0.5 L/min airflow (Experiment D), MB diameters were 75–160 µm (mean 102.60 µm; SD 19.91 µm) and rise velocities 0.1×10⁴–2.7×10⁴ µm/s (mean 1.28×10⁴ µm/s; SD 6.31×10³ µm/s). Across all four experiments, mean MB diameters remained below 200 µm and mean rise velocities below 2.1×10⁴ µm/s. Notably, the 36 psi/ 0.1 L/min condition produced the smallest mean diameters and among the lowest velocities (< 1×10⁴ µm/s), while the 36 psi/ 0.5 L/min and 34 psi/ 0.1 L/min conditions also yielded mean diameters < 120 µm and mean velocities < 1.4×10⁴ µm/s. These three operating combinations, therefore, represent the most favorable ranges, within those tested, for generating relatively small and slow-rising MBs.

The reproducibility of results was assessed through repeated tests, showing consistency with findings from similar studies. Specifically, reducing bubble size results in a decrease in rise velocity, which contrasts with the phenomenon that rise velocity increases as bubble size grows. This trend is illustrated in Figure 9, which shows the rise velocities of three microbubbles with different diameters. The microbubble with a diameter of 83.64 µm has a lower rise velocity than those with diameters of 89.64 µm and 102 µm. This fact occurs because smaller microbubbles contain less oxygen and move more slowly. The velocities of all three microbubbles show fluctuations, likely due to fluid turbulence during ascent, which may be caused by hydrodynamic cavitation. This turbulence can lead to collisions between microbubbles, resulting in

sudden changes in trajectory or speed. Furthermore, prior work on hydrodynamic-cavitation systems has reported that bubbles may nucleate and migrate near confining walls, where the wettability of those surfaces (hydrophobic vs. hydrophilic) can influence bubble stability, coalescence behavior, and resulting size distributions [50]. Such near-wall wettability effects could contribute to the variability in microbubble diameters observed across our operating conditions and merit targeted investigation in future work.

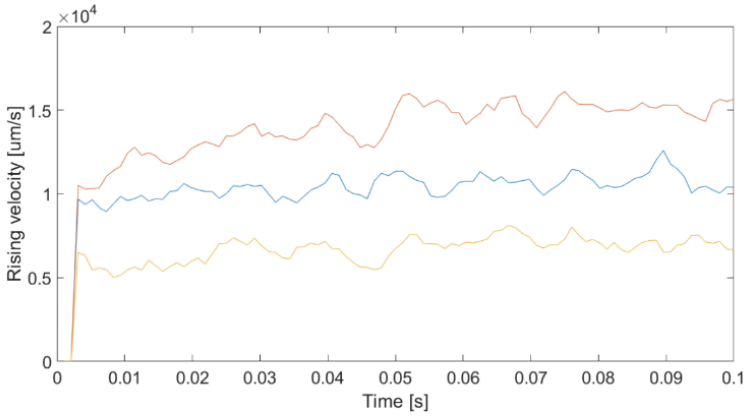

Figure 9. Example of three microbubbles speed behavior with different diameters

Based on the results, this research determined the diameter and rise velocity of microbubbles generated in a laboratory-scale DAF tank, focusing on the turbulence primarily produced in the contact chamber where water flow and microbubbles mix intensively. In DAF systems, turbulence is crucial for ensuring the uniform distribution of air bubbles, which allows suspended particles to adhere to the bubbles and form MB-particle clusters. Therefore, an increase in the air-water ratio is expected to enhance the bubble coalescence rate [51]. Each experiment indirectly demonstrated that MB formation primarily depends on the pressure set for the DAF system's pressurized water and recirculation pressure, with smaller microbubble diameters observed at recirculation pressures of 0.1 L/min as shown in Table 4.

Table 4. Diameters and rise velocities of microbubbles for each experiment

Experiment	Air injection rates [L/min]	Saturation Pressure [psi]	Diameters [µm]	Rise velocity [µm/s]
A	0.1	34	117.34	1.35×10^4
B	0.5	34	165.32	2.04×10^4
C	0.1	36	98.65	9.89×10^3
D	0.5	36	102.60	1.28×10^4

Different studies have addressed bubble characterization in DAF systems; however, the impact of operational parameters, such as recirculation flow rate and saturation pressure, on bubble generation has yet to be thoroughly detailed. Additionally, studies in the literature often examine DAF bubbles in flotation columns, where bubble characterization is more optimal due to hydrodynamics that better align with the bubbles' natural upward movement. In contrast, rectangular flotation tanks present more complex hydrodynamics. Furthermore, DAF systems typically utilize microbubble generation pumps, which yield optimal results but are costly. This study, however, utilized a Venturi tube for microbubble generation due to its simplicity and low cost.

For example, in [52], a laboratory-scale DAF column reactor was designed to evaluate the removal of total suspended solids and measure bubble size. Bubble diameters were calculated based on velocity data and Stokes' equation; however, this equation assumes that the bubbles are spherical, have a smooth surface, and flow in laminar conditions. The horizontal and vertical velocity components of each frame were extracted using particle image velocimetry. In [13], high-speed photography in a rectangular DAF tank system was used to characterize microbubble size and rise velocity. However, this system used a generation method distinct from the Venturi tube, with effluent flow control and temperature regulation between 15–20 °C. In Swart *et al.* [53] used the same system to simultaneously monitor flow patterns and the characteristics of bubbles and plastic microparticles in DAF. The horizontal and vertical coordinates, as well

as the bubble diameter, were recorded to track bubbles across consecutive images and calculate their rise velocity. However, the authors did not address the presence of overlapping microbubbles.

Compared with previous DAF studies that relied on high-speed industrial cameras [13], [52], [53] or on indirect size inference from Stokes-law assumptions under ideal, laminar conditions [52], the present work achieves comparable measurement ranges while using a low-cost Huawei P30 smartphone, a Venturi injector, and a conventional 2 HP water pump that recirculates tap water at up to 16 L min^{-1} and 34–36 psi. Under identical hydraulic conditions, the proposed algorithm resolves MB overlap caused by turbulence, an issue not addressed in earlier studies, through frame-by-frame centroid tracking with a Euclidean-distance gate (Section 2.4). In the rectangular-tank geometry used, mean diameters of 99–165 µm and rise velocities of 9.9×10^3–2.0×10^4 µm s^{-1} as shown in Table 4 fall within, or improve upon, the ranges reported for column reactors (67–400 µm and 1.1×10^4–3.5×10^4 µm s^{-1}) while avoiding the over-segmentation and high computational cost associated with watershed-based pipelines [32], [46], [47]. These results demonstrate that the proposed image-processing configuration. Table 2 shows provide a practical and cost-effective alternative for MB characterization in the more hydrodynamically complex and industrially standard rectangular DAF tanks, with the added advantage of robust performance under high recirculation flow and turbulent overlap.

4. CONCLUSION

A low-cost computer-vision system was developed in MATLAB to quantify microbubble (MB) diameter and rise velocity in a laboratory-scale DAF tank. The pipeline combines grayscale conversion, Median, Gaussian, and local-Laplacian filtering, gamma contrast enhancement, Otsu segmentation, morphological refinement, and Circular Hough detection. MB trajectories are reconstructed by linking centroids frame-to-frame with a Euclidean distance gate, allowing for reliable measurement even when bubbles overlap in turbulent flow. Under the four operating conditions examined, the 36 psi/ 0.1 L/min setting produced the smallest mean diameter (~99 µm) and the lowest mean rise velocity (~9.9×10^3 µm/s), confirming that smaller bubbles rise more slowly and therefore remain available longer for particle capture.

Compared to earlier DAF studies that relied on high-speed industrial cameras, Stokes-law assumptions, or computationally intensive watershed segmentation, the proposed smartphone-based approach achieves similar measurement ranges while resolving bubble overlap and significantly reducing cost and complexity. The observed variability in MB size across conditions suggests that factors such as surface wettability, fluid chemistry, and temperature may further influence bubble nucleation and coalescence. Future work will investigate these variables and scale the algorithm to full-size DAF units to validate its practicality for on-site monitoring and process optimization.

ACKNOWLEDGEMENTS

The authors thank the Hydraulics Laboratory and the Master's Program in Automation at the University of Cauca for their assistance in the experimental setup.

FUNDING INFORMATION

This work received no specific grant from funding agencies in the public, commercial, or not-for-profit sectors. The study was carried out using the facilities and routine resources of the Hydraulics Laboratory at Universidad del Cauca.

AUTHOR CONTRIBUTIONS STATEMENT

This journal uses the Contributor Roles Taxonomy (CRediT) to recognize individual author contributions, reduce authorship disputes, and facilitate collaboration.

Name of Author	C	M	So	Va	Fo	I	R	D	O	E	Vi	Su	P	Fu
Jeimmy Adriana Muñoz Alegría	✓	✓	✓	✓	✓	✓		✓	✓	✓	✓			
Jesús Emilio Pinto-Lopera	✓	✓	✓	✓	✓	✓		✓	✓	✓	✓	✓		
Elena Muñoz-España	✓			✓			✓			✓	✓		✓	✓
Juan Fernando Flórez-Marulanda	✓			✓			✓			✓	✓		✓	✓

C : **C**onceptualization	I : **I**nvestigation	Vi : **Vi**sualization
M : **M**ethodology	R : **R**esources	Su : **Su**pervision
So : **So**ftware	D : **D**ata Curation	P : **P**roject administration
Va : **Va**lidation	O : Writing - **O**riginal Draft	Fu : **Fu**nding acquisition
Fo : **Fo**rmal analysis	E : Writing - Review & **E**diting	

CONFLICT OF INTEREST STATEMENT

Authors state no conflict of interest.

DATA AVAILABILITY

The authors confirm that the data supporting the findings of this study are available within the article and its figures. Additional raw videos are available from the corresponding author upon reasonable request.

REFERENCES

[1] E. Koncagül, M. Tran, R. Connor, and S. Uhlenbrook, "The United Nations world water development report 2019: leaving no one behind, facts and figures," *UNESCO*, 2019. https://unesdoc.unesco.org/ark:/48223/pf0000367276_spa

[2] UNESCO, "The United Nations world water development report 2021: valuing water," *UNESCO World Water Assessment Programme*, 2021. https://www.unesco.org/reports/wwdr/2021/en/download-report

[3] E. R. Jones, M. T. H. Van Vliet, M. Qadir, and M. F. P. Bierkens, "Country-level and gridded estimates of wastewater production, collection, treatment and reuse," *Earth System Science Data*, vol. 13, no. 2, pp. 237–254, 2021, doi: 10.5194/essd-13-237-2021.

[4] W. Chung and S. Young, "Evaluation of a chemical dissolved air flotation system for the treatment of restaurant dishwasher effluent," *Canadian Journal of Civil Engineering*, vol. 40, no. 12, pp. 1164–1172, 2013, doi: 10.1139/cjce-2012-0357.

[5] R. Prakash, S. K. Majumder, and A. Singh, "Flotation technique: Its mechanisms and design parameters," *Chemical Engineering and Processing - Process Intensification*, vol. 127, pp. 249–270, 2018, doi: 10.1016/j.cep.2018.03.029.

[6] M. Zhang and P. Guiraud, "Surface-modified microbubbles (colloidal gas aphrons) for nanoparticle removal in a continuous bubble generation-flotation separation system," *Water Research*, vol. 126, pp. 399–410, 2017, doi: 10.1016/j.watres.2017.09.051.

[7] F. A. Soares *et al.*, "Dissolved air flotation as potential new mechanism for intestinal parasite diagnosis in feces," *Acta Tropica*, vol. 224, p. 106137, 2021, doi: 10.1016/j.actatropica.2021.106137.

[8] M. Qadafi, S. Notodarmojo, and Y. Zevi, "Effects of microbubble pre-ozonation time and pH on trihalomethanes and haloacetic acids formation in pilot-scale tropical peat water treatments for drinking water purposes," *Science of the Total Environment*, vol. 747, p. 141540, 2020, doi: 10.1016/j.scitotenv.2020.141540.

[9] X. Luo, H. Gong, Z. He, P. Zhang, and L. He, "Recent advances in applications of power ultrasound for petroleum industry," *Ultrasonics Sonochemistry*, vol. 70, p. 105337, 2021, doi: 10.1016/j.ultsonch.2020.105337.

[10] Z. Sun *et al.*, "Innovative process for total petroleum hydrocarbons reduction on oil refinery sludge through microbubble ozonation," *Journal of Cleaner Production*, vol. 256, p. 120337, 2020, doi: 10.1016/j.jclepro.2020.120337.

[11] K. A. Tan, Y. Mohan, K. J. Liew, S. H. Chong, and P. E. Poh, "Development of an effective cleaning method for metallic parts using microbubbles," *Journal of Cleaner Production*, vol. 261, p. 121076, 2020, doi: 10.1016/j.jclepro.2020.121076.

[12] L. Jothinathan, Q. Q. Cai, S. L. Ong, and J. Y. Hu, "Organics removal in high strength petrochemical wastewater with combined microbubble-catalytic ozonation process," *Chemosphere*, vol. 263, p. 127980, 2021, doi: 10.1016/j.chemosphere.2020.127980.

[13] B. Swart *et al.*, "In situ characterisation of size distribution and rise velocity of microbubbles by high-speed photography," *Chemical Engineering Science*, vol. 225, p. 115836, 2020, doi: 10.1016/j.ces.2020.115836.

[14] T. Temesgen, T. T. Bui, M. Han, T. il Kim, and H. Park, "Micro and nanobubble technologies as a new horizon for water-treatment techniques: A review," *Advances in Colloid and Interface Science*, vol. 246, pp. 40–51, 2017, doi: 10.1016/j.cis.2017.06.011.

[15] J. O. Hanotu, H. Bandulasena, and W. B. Zimmerman, "Aerator design for microbubble generation," *Chemical Engineering Research and Design*, vol. 123, pp. 367–376, 2017, doi: 10.1016/j.cherd.2017.01.034.

[16] H. Sun, H. Liu, S. Wang, and Y. Liu, "Remediation of oil spill-contaminated sands by chemical-free microbubbles generated in tap and saline water," *Journal of Hazardous Materials*, vol. 366, pp. 124–129, 2019, doi: 10.1016/j.jhazmat.2018.11.102.

[17] S. J. Gulden, C. Riedele, S. Rollié, M. H. Kopf, and H. Nirschl, "Online bubble size analysis in micro flotation," *Chemical Engineering Science*, vol. 185, pp. 168–181, 2018, doi: 10.1016/j.ces.2018.04.009.

[18] M. Lichti and H. J. Bart, "Bubble size distributions with a shadowgraphic optical probe," *Flow Measurement and Instrumentation*, vol. 60, pp. 164–170, 2018, doi: 10.1016/j.flowmeasinst.2018.02.020.

[19] L. Vinnett, J. Sovechles, C. O. Gomez, and K. E. Waters, "An image analysis approach to determine average bubble sizes using one-dimensional Fourier analysis," *Minerals Engineering*, vol. 126, pp. 160–166, 2018, doi: 10.1016/j.mineng.2018.06.030.

[20] W. E. Juwana, A. Widyatama, O. Dinaryanto, W. Budhijanto, Indarto, and Deendarlianto, "Hydrodynamic characteristics of the microbubble dissolution in liquid using orifice type microbubble generator," *Chemical Engineering Research and Design*, vol. 141, pp. 436–448, 2019, doi: 10.1016/j.cherd.2018.11.017.

[21] X. Tao, Y. Liu, H. Jiang, and R. Chen, "Microbubble generation with shear flow on large-area membrane for fine particle flotation," *Chemical Engineering and Processing - Process Intensification*, vol. 145, p. 107671, 2019, doi: 10.1016/j.cep.2019.107671.

[22] K. Ruby and S. K. Majumder, "Studies on stability and properties of micro and nano-particle-laden ionic microbubbles," *Powder Technology*, vol. 335, pp. 77–90, 2018, doi: 10.1016/j.powtec.2018.04.069.

[23] R. Pérez-Garibay, A. Bueno-Tokunaga, R. H. Estrada-Ruiz, and L. F. Camacho-Ortegón, "Effect of surface electrical charge on microbubbles' terminal velocity and gas holdup," *Minerals Engineering*, vol. 119, pp. 166–172, 2018, doi: 10.1016/j.mineng.2018.01.026.

[24] A. Gordiychuk, M. Svanera, S. Benini, and P. Poesio, "Size distribution and Sauter mean diameter of micro bubbles for a Venturi type

bubble generator," *Experimental Thermal and Fluid Science*, vol. 70, pp. 51–60, 2016, doi: 10.1016/j.expthermflusci.2015.08.014.
[25] L. R. Villegas, D. Colombet, P. Guiraud, D. Legendre, S. Cazin, and A. Cockx, "Image processing for the experimental investigation of dense dispersed flows: Application to bubbly flows," *International Journal of Multiphase Flow*, vol. 111, pp. 16–30, 2019, doi: 10.1016/j.ijmultiphaseflow.2018.10.017.
[26] L. Zhao *et al.*, "A visualized study of the motion of individual bubbles in a venturi-type bubble generator," *Progress in Nuclear Energy*, vol. 97, pp. 74–89, 2017, doi: 10.1016/j.pnucene.2017.01.004.
[27] F. Noelle, M. R. Molteno, and R. W. M. Pott, "Calibrated bubble depth determination using a single camera," *Chemical Engineering Research and Design*, vol. 164, pp. 11–22, 2020, doi: 10.1016/j.cherd.2020.09.023.
[28] R. F. L. Cerqueira and E. E. Paladino, "Development of a deep learning-based image processing technique for bubble pattern recognition and shape reconstruction in dense bubbly flows," *Chemical Engineering Science*, vol. 230, p. 116163, 2021, doi: 10.1016/j.ces.2020.116163.
[29] J. Ilonen *et al.*, "Comparison of bubble detectors and size distribution estimators," *Pattern Recognition Letters*, vol. 101, pp. 60–66, 2018, doi: 10.1016/j.patrec.2017.11.014.
[30] M. A. Seger, C. Oliveira, and R. T. Rodrigues, "Development of a laboratory-scale flotation column with inlet bubble size measurement," *Minerals Engineering*, vol. 142, p. 105936, 2019, doi: 10.1016/j.mineng.2019.105936.
[31] N. N. Misra, R. Phalak, and A. Martynenko, "A microscopic computer vision algorithm for autonomous bubble detection in aerated complex liquids," *Journal of Food Engineering*, vol. 238, pp. 54–60, 2018, doi: 10.1016/j.jfoodeng.2018.06.007.
[32] H. Zhang, Z. Tang, Y. Xie, X. Gao, and Q. Chen, "A watershed segmentation algorithm based on an optimal marker for bubble size measurement," *Measurement: Journal of the International Measurement Confederation*, vol. 138, pp. 182–193, 2019, doi: 10.1016/j.measurement.2019.02.005.
[33] U. Iben, F. Wolf, H. A. Freudigmann, J. Fröhlich, and W. Heller, "Optical measurements of gas bubbles in oil behind a cavitating micro-orifice flow," *Experiments in Fluids*, vol. 56, no. 6, pp. 1–10, 2015, doi: 10.1007/s00348-015-1979-6.
[34] H. Zhou and X. Niu, "An image processing algorithm for the measurement of multiphase bubbly flow using predictor-corrector method," *International Journal of Multiphase Flow*, vol. 128, p. 103277, 2020, doi: 10.1016/j.ijmultiphaseflow.2020.103277.
[35] V. R. Fanaie and M. Khiadani, "Effect of salinity on air dissolution, size distribution of microbubbles, and hydrodynamics of a dissolved air flotation (DAF) system," *Colloids and Surfaces A: Physicochemical and Engineering Aspects*, vol. 591, p. 124547, 2020, doi: 10.1016/j.colsurfa.2020.124547.
[36] S. Unyaphan, T. Tarnpradab, F. Takahashi, and K. Yoshikawa, "Improvement of tar removal performance of oil scrubber by producing syngas microbubbles," *Applied Energy*, vol. 205, pp. 802–812, 2017, doi: 10.1016/j.apenergy.2017.08.071.
[37] S. Schmideder, L. Thurin, G. Kaur, and H. Briesen, "Inline imaging reveals evolution of the size distribution and the concentration of microbubbles in dissolved air flotation," *Water Research*, vol. 224, p. 119027, 2022, doi: 10.1016/j.watres.2022.119027.
[38] S. G. Da Cruz, A. J. B. Dutra, and M. B. M. Monte, "The influence of some parameters on bubble average diameter in an electroflotation cell by laser diffraction method," *Journal of Environmental Chemical Engineering*, vol. 4, no. 3, pp. 3681–3687, 2016, doi: 10.1016/j.jece.2016.05.017.
[39] K. Bae, G. S. Go, N. S. Noh, Y. Il Lim, J. W. Bae, and D. H. Lee, "Bubble characteristics in pressurized bubble column associated with micro-bubble dispersion," *Chemical Engineering Journal*, vol. 386, 2020, doi: 10.1016/j.cej.2019.03.215.
[40] O. Adetunji and R. Rawatlal, "Estimation of bubble column hydrodynamics: Image-based measurement method," *Flow Measurement and Instrumentation*, vol. 53, pp. 4–17, 2017, doi: 10.1016/j.flowmeasinst.2016.08.002.
[41] K. Li, Q. Wang, and M. Wang, "Three-dimensional visualisation of gas-water two-phase flow based on bubble mapping method and size projection algorithm," *Flow Measurement and Instrumentation*, vol. 69, p. 101590, 2019, doi: 10.1016/j.flowmeasinst.2019.101590.
[42] S. Haris, X. Qiu, H. Klammler, and M. M. A. Mohamed, "The use of micro-nano bubbles in groundwater remediation: A comprehensive review," *Groundwater for Sustainable Development*, vol. 11, p. 100463, 2020, doi: 10.1016/j.gsd.2020.100463.
[43] Y. Xiong and F. Peng, "Optimization of cavitation venturi tube design for pico and nano bubbles generation," *International Journal of Mining Science and Technology*, vol. 25, no. 4, pp. 523–529, 2015, doi: 10.1016/j.ijmst.2015.05.002.
[44] X. Chen *et al.*, "Fourier-transform-based two-stage camera calibration method with simple periodical pattern," *Optics and Lasers in Engineering*, vol. 133, p. 106121, 2020, doi: 10.1016/j.optlaseng.2020.106121.
[45] Q. Zhang, H. Xie, W. Shi, and B. Fan, "A novel sampling moiré method and its application for distortion calibration in scanning electron microscope," *Optics and Lasers in Engineering*, vol. 127, p. 105990, 2020, doi: 10.1016/j.optlaseng.2019.105990.
[46] L. Vinnett, J. Yianatos, L. Arismendi, and K. E. Waters, "Assessment of two automated image processing methods to estimate bubble size in industrial flotation machines," *Minerals Engineering*, vol. 159, p. 106636, 2020, doi: 10.1016/j.mineng.2020.106636.
[47] P. K. Saha, R. Pal, S. Sarkar, and A. Mukhopadhyay, "A novel image processing technique for detection of pseudo occluded bubbles and identification of flow regimes in a bubble column reactor," *Measurement: Journal of the International Measurement Confederation*, vol. 189, p. 110568, 2022, doi: 10.1016/j.measurement.2021.110568.
[48] X. Wang, C. Song, C. Yang, and Y. Xie, "Process working condition recognition based on the fusion of morphological and pixel set features of froth for froth flotation," *Minerals Engineering*, vol. 128, pp. 17–26, 2018, doi: 10.1016/j.mineng.2018.08.017.
[49] A. Eskanlou, M. R. Khalesi, M. Mirmogaddam, M. Hemmati Chegeni, and B. Vaziri Hassas, "Investigation of trajectory and rise velocity of loaded and bare single bubbles in flotation process using video processing technique," *Separation Science and Technology (Philadelphia)*, vol. 54, no. 11, pp. 1795–1802, 2019, doi: 10.1080/01496395.2018.1539104.
[50] P. D. Desai and W. B. Zimmerman, "Transient effects and the role of wetting in microbubble generation," *Current Opinion in Colloid and Interface Science*, vol. 67, p. 101722, 2023, doi: 10.1016/j.cocis.2023.101722.
[51] F. A. Hamad, K. Pun, B. Alessio, S. A. Najim, P. B. Ganesan, and D. Hughes, "Experimental measurements on the microbubble characteristics and dissolved oxygen (DO) in water using single and twin-Venturi type microbubble generators," *Chemical Engineering Science*, vol. 280, p. 118994, 2023, doi: 10.1016/j.ces.2023.118994.
[52] A. L. Piaggio, G. Smith, M. K. de Kreuk, and R. E. F. Lindeboom, "Application of a simplified model for assessing particle removal in dissolved air flotation (DAF) systems: Experimental verification at laboratory and full-scale level," *Separation and Purification Technology*, vol. 340, p. 126801, 2024, doi: 10.1016/j.seppur.2024.126801.
[53] B. Swart, Y. M. J. Chew, and J. Wenk, "Simultaneous monitoring of flow patterns, and bubble, and plastics micro-particle characteristics in dissolved air flotation (DAF)," *Chemical Engineering Research and Design*, vol. 197, pp. 148–158, 2023, doi: 10.1016/j.cherd.2023.07.027.

BIOGRAPHIES OF AUTHORS

Jeimmy Adriana Muñoz Alegría received her degree in physical engineering from the University of Cauca in 2017 and a master's degree in automatic control from the same university in 2022. Currently, she is a Ph.D. student in energy, water and environment at the University of La Serena, Chile. Her research interests include renewable energy, water quality, machine learning, water resources, wastewater treatment systems, automation and control, data analysis and treatment, and engineering projects applying engineering and artificial intelligence to solutions to current water and environmental problems. She can be contacted at email: jeimmy.munoz@userena.cl.

Jesús Emilio Pinto-Lopera received his degree in physical engineering from the University of Cauca (Colombia) in 2007. He completed postgraduate studies at the University of Brasília in Brazil and holds a master's and doctorate in mechatronic systems. His areas of expertise include artificial intelligence and applied physics. He is currently a full professor in the systems engineering program at the University of Amazonia, Colombia. His research interests include computer vision and intelligent systems. At the University of Amazonia, he is a leader of Group of Research in Engineering and Nature (GREEN). He can be contacted at: jes.pinto@udla.edu.co.

Elena Muñoz-España received the engineering degree in electronics and telecommunications engineering, and master's degree in electronics engineering from Universidad del Cauca. She is currently working as a full professor at the University of Cauca, Colombia. Her research interests include control systems, computer vision and medical image processing. She can be contacted at email: elenam@unicauca.edu.co.

Juan Fernando Flórez-Marulanda received a degree in electronics and telecommunications engineering, specializing in telematics networks and services and industrial computing, as well as a master's degree in electronics engineering from Universidad del Cauca. He teaches at Universidad del Cauca since 1998, guiding subjects involving instrumentation, control, computer vision, and automation while advising degree works related to ISA, ISO, and IEEE standards and industrial process automation methodologies. He can be contacted at email: jflorez@unicauca.edu.co.